

Diurnal Cycle of Rainfall and Winds near the South Coast of China

YU DU

Center for Monsoon and Environment Research, School of Atmospheric Sciences, and Guangdong Province Key Laboratory for Climate Change and Natural Disaster Studies, Sun Yat-sen University, Guangzhou, China

RICHARD ROTUNNO

National Center for Atmospheric Research, Boulder, Colorado

(Manuscript received 27 December 2017, in final form 6 March 2018)

ABSTRACT

The characteristics and mechanisms of diurnal rainfall and winds near the south coast of China are explored using satellite data (CMORPH), long-term hourly WRF Model data (Du model data), a simple 2D linear model, and 2D idealized simulations. Both the CMORPH and Du model data indicate that the diurnal cycle of rainfall has two propagation modes near the coast: onshore and offshore. The diurnally periodic winds (vertical motions) also show a similar propagation feature. Analysis of the rainfall budget indicates that vertically integrated vertical vapor advection plays a key role in the diurnal cycle of rainfall and thus provides a physical connection between winds and rainfall in the diurnal cycle. It was found that a simple 2D linear land–sea breeze model with a background wind can well capture the two propagation modes, which are associated with inertia–gravity waves, in terms of speed and phase. The background wind changes the pattern of the inertia–gravity waves and further affects the diurnal propagation. The effect of the background wind on the diurnal propagation was verified through idealized simulations using a simplified version of the WRF Model that can also capture the diurnal features.

1. Introduction

The diurnal cycle of precipitation is a very important aspect of weather and regional climate (e.g., Dai and Deser 1999; Yang and Smith 2006) and has been extensively studied all over the world through observations (e.g., Yang and Slingo 2001) and numerical simulations (e.g., Garreaud and Muñoz 2004). The diurnal cycle is a fundamental mode of precipitation variability and provides opportunities for testing our understanding and modeling of the governing physical processes and their multiscale interactions. The most prominent diurnal variations of precipitation commonly manifest as propagating cloud disturbances and often occur in the lee of continental mountain ranges, such as the Rocky Mountains (Carbone et al. 2002; Trier et al. 2006), the Andes (Romatschke and Houze 2010; Rasmussen and Houze 2011), and the Tibetan Plateau (Wang et al. 2004; Bao et al. 2011; Du et al. 2014; Sun and Zhang 2012); and off coasts, such as the Panama

Bight region (Mapes et al. 2003), New Guinea (Hassim et al. 2016), and Darwin (Wapler and Lane 2012), and others (Mori et al. 2004; Li and Carbone 2015).

A number of studies attribute the diurnal propagation of precipitation to convective systems originating from the mountain–plains solenoid (MPS; Carbone and Tuttle 2008; He and Zhang 2010, Bao et al. 2011) associated with upstream mountains or to the land–sea breeze (Li and Carbone 2015; Zhu et al. 2017) in coastal areas. However, Chen et al. (2012) suggested that the eastward-delayed diurnal phase of rainfall down the Yangtze River valley (in the lee of the Tibetan Plateau) is due to the diurnal clockwise rotation of the low-level winds under the Coriolis force. Nocturnal low-level jets and diurnal monsoon flows transporting warm/moist air or interacting with a quasi-stationary lower-tropospheric front may also be responsible for the nocturnal rainfall in the lee of the Rocky Mountains and the Tibetan Plateau (Trier et al. 2014; Chen et al. 2009, 2013). Another popular mechanism for diurnal propagation is through the action of gravity waves near the tropical coast. Mapes et al. (2003) found that a propagation signal (convection) in the Panama Bight region off the northwestern coast of South America is due to thermally

Corresponding author address: Associate Professor Yu Du, duyu7@mail.sysu.edu.cn

forced gravity waves produced by elevated terrain. Houze (2004) proposed a similar diurnally generated wave propagation over the Bay of Bengal. Gravity waves were observed by an instrumented ship during the Joint Air–Sea Monsoon Interaction Experiment (JASMINE; Webster et al. 2002). Gille et al. (2005), using four-times-daily sea surface winds, found that the diurnal perturbations of sea surface winds propagate progressively offshore at speeds ranging from 2 to 15 m s^{-1} , resembling gravity waves. Yang and Slingo (2001) using brightness temperatures from multiple satellites, found that a strong signal over land in the tropics, such as in the diurnal cycles of convection, cloudiness and surface temperature, can propagate several hundreds of kilometers over the adjacent ocean. Hassim et al. (2016) investigated the occurrence and dynamics of offshore-propagating convective systems that contribute to the observed early-morning rainfall maximum northeast of New Guinea, Australia, and also highlighted the importance of terrain, coastal effects, and gravity waves. Kilpatrick et al. (2017) utilized satellite observations of surface winds and rainfall to show the offshore copropagation of the land breeze and diurnal rainfall signals 300–400 km from the east coast of India into the Bay of Bengal, and found that the surface-wind-convergence maximum leads the rainfall maximum by 1–2 h, implying that the land–sea breeze forces the diurnal cycle of rainfall.

Heavy rainfall frequently occurs over the south coast of China, causing large economic and human losses. The diurnal cycle of rainfall and its propagation signals over this region were observed with rain gauge, radar, and satellite data (Aves and Johnson 2008; Chen et al. 2015; Chen et al. 2018; Jiang et al. 2017). Chen et al. (2016) found that the nocturnal offshore rainfall over the south China coastal region is related to the convergence line between the prevailing low-level monsoonal wind and the land breeze, while rainfall propagates inland with the inland penetration of the sea breeze in the daytime and the help of the cold-pool dynamics. Thus, the pattern of coastal-rainfall spatial distribution is controlled by the ambient onshore wind speed (Chen et al. 2017). Using CMORPH (see below) data, Jiang et al. (2017) found an inland-propagation mode of rainfall occurs in the daytime that can be related to land–sea breeze along the southern coastal region. However, the present study shows that a simple land–sea breeze model is not sufficient to explain the observed propagation speed. Therefore, this study looks in detail at the mechanism(s) of the diurnal propagation near the south coast of China through a combination of observations, modeling, and theory.

Du and Rotunno (2015), using a long-term daily-simulation dataset (Du et al. 2014, 2015a,b, called the “Du model data”), found that a simple 2D linear land–sea breeze

model with friction can capture the wind-propagation signals off the east coast of China. Linear theory has been widely used to study the atmospheric response to land–sea differential heating (Rotunno 1983; Qian et al. 2009; Drobinski et al. 2011) and the dynamics of offshore diurnal waves induced by a land–sea thermal contrast (Jiang 2012a,b; Li and Carbone 2015). Qian et al. (2009) include a uniform background wind for $f = 0$ (the equator; f is the Coriolis parameter) in the solution that introduces Doppler shifting and wave dispersion effects. Li and Carbone (2015), based on their linear model, further proposed that the diurnal propagation of rainfall offshore of India over the Bay of Bengal and a diurnal, but nonpropagating, signal on the eastern side of the bay near the west coast of Burma might be related to the steering wind.

Therefore, in the present study, we attempt to use CMORPH data, Du model data, linear theory with a background wind, and a 2D idealized WRF Model simulation to explain the main diurnal-propagation features of rainfall near the south coast of China. In section 2 features of the diurnal rainfall propagation near the south coast of China are described using CMORPH data. In section 3 the diurnal cycle of rainfall from the Du model data is compared with the CMORPH data and the propagation signals are analyzed through their wind and rainfall budgets. An explanation in terms of linear land–sea breezes, including a background wind, is discussed in section 4. In section 5 an idealized version of the WRF Model is utilized to confirm the effect of a background wind derived from the linear model. The results are summarized in section 6.

2. Diurnal cycle of rainfall from the CMORPH data

a. The CMORPH data

The Climate Prediction Center morphing technique (CMORPH) rainfall data have a high spatial (8 km) and temporal (30 min) resolution, which uses rainfall estimates from both low-orbiter satellite microwave observation and geostationary satellite IR data. The CMORPH data have been extensively used to study the diurnal cycle of rainfall over China and its vicinity (e.g., Jiang et al. 2017; He and Zhang 2010; Bao et al. 2011; Zhu et al. 2017). Compared with finescale rain gauge data, the CMORPH data well resolve morning rainfall at the coasts, and afternoon rainfall on the land, of southern China (although the CMORPH data tend to underestimate the morning rainfall at coastal sites and overestimate the afternoon rainfall at inland sites; Chen et al. 2018). The CMORPH data used in this study cover the month of June in the years 1998–2015.

b. Features of diurnal rainfall

Using the CMORPH data, we focus on the characteristics of diurnal rainfall on and off the south coast of China, such as the time phase and amplitude of the diurnal cycle and the propagation signals.

Figure 1 shows the local standard time (LST) of maximum rainfall near the south coast of China: the rainfall peaks in the afternoon and evening over the land, and in the morning off the south coast. The diurnal cycle of rainfall near the south coast of China has two modes of propagation: offshore-directed propagation over the ocean and onshore-directed propagation over the land. To see those features clearly, distance (latitude)–time Hovmöller diagrams of hourly precipitation deviations averaged over the black box (Fig. 1) are shown in Fig. 2a. Note that hourly precipitation deviation ($r_t - \bar{r}$) is estimated as the mean rainfall rate at the current hour minus the mean rainfall rate throughout the day. Over the ocean, the maximum rainfall occurs at around 0800 LST near the coast and propagates southward to 300 km away from the coast around 1300 LST. Over the land, the rainfall near the coast reaches a maximum at noon (around 1200 LST) and propagates northward (inland) through the afternoon. The offshore propagation speed over the ocean is around 16 m s^{-1} , whereas the onshore propagation speed over the land is around 22 m s^{-1} . Following He and Zhang (2010) and Du et al. (2014), distance (latitude)–time Hovmöller diagrams of normalized hourly precipitation deviations averaged over the black box (Fig. 1) are shown in Fig. 2b in order to present these two propagation modes more clearly. Note that hourly precipitation deviation $[(r_t - \bar{r})/\sigma]$ is estimated as the mean rainfall rate at the current hour minus the mean rainfall rate throughout the day, normalized by the standard deviation of hourly rainfall at each point.

These propagation features may be associated with the inertia–gravity wave response to diurnal heating at low latitudes ($0^\circ\text{--}30^\circ$) proposed by Du and Rotunno (2015) in their analysis of the diurnal winds at low levels off the east coast of China with the Du model data. Therefore, in the next section, we attempt to use the Du model data to analyze the diurnal cycle of rainfall and winds, and their relation near the south coast of China.

3. Diurnal cycle from the Du model data

a. Review of the Du model data

The Du model data are hourly model data (9-km horizontal grid spacing and 40 vertical levels) covering all of China ($6030 \text{ km} \times 6030 \text{ km}$) for the warm season in 2006–11 simulated with the Advanced Research version of the Weather Research and Forecasting Model

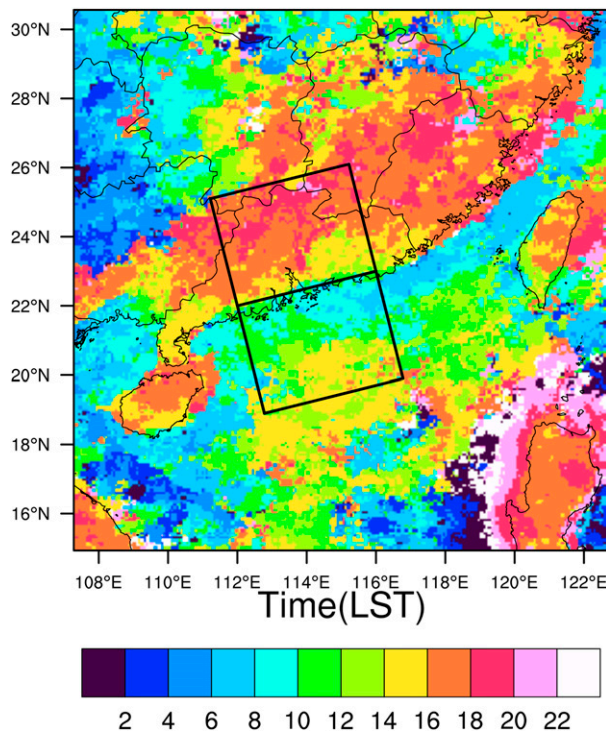


FIG. 1. Time of maximum rainfall (LST) for 18 years (1998–2015) using the CMORPH data; the black boxes are used for the analysis in Fig. 2.

(WRF-ARW; Skamarock and Klemp 2008) from 12- to 36-h simulations of each day. The physical parameterizations used include the Kain–Fritsch convective parameterization scheme, the Yonsei University (YSU) boundary layer scheme, WRF single-moment 6-class graupel, the RRTM longwave radiation and the Dudhia shortwave radiation schemes, the Monin–Obukhov surface-layer scheme, and the unified Noah land surface model scheme. Model verification against long-record observations and the detailed model configuration and integration procedures are given in Du et al. (2014). This dataset has been utilized in the study of low-level jets and low-level winds over China (Du et al. 2014, 2015a,b) and can capture the diurnal propagation signals east of the Tibetan Plateau (section 5b in Du et al. 2014) and off the east coast of China (Du and Rotunno 2015).

b. Characteristics of the diurnal rainfall and winds

Figure 3 shows the Hovmöller diagrams of hourly precipitation deviations and normalized hourly precipitation deviations averaged over the black box (Fig. 1) from the CMORPH (Figs. 3a,b) and the Du model data (Figs. 3c,d) during the same period (June 2006–11). Two propagation modes of rainfall (offshore and onshore) exist in the Du model data, similar to the features from the CMORPH data, although the

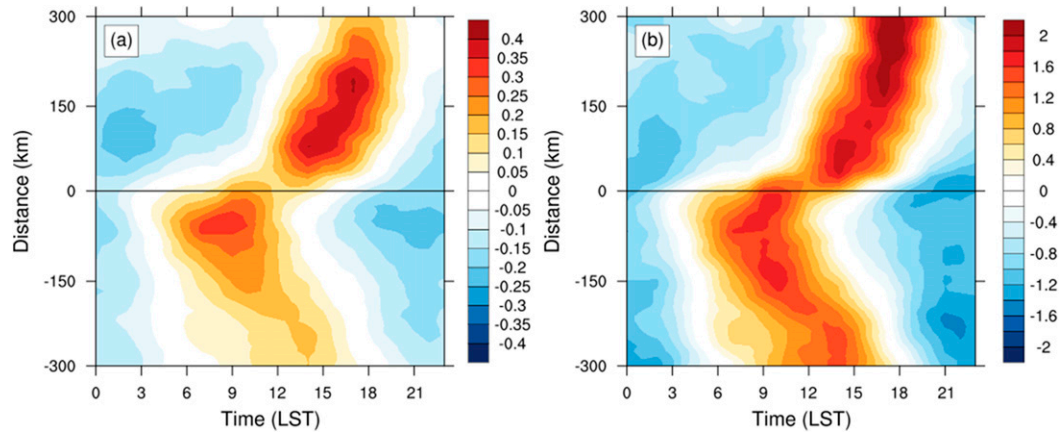


FIG. 2. Distance (latitude)-time Hovmöller diagrams of (a) hourly precipitation deviations (mm) and (b) normalized hourly precipitation deviations during June from 1998 to 2015 averaged over the black boxes in Fig. 1 from the CMORPH data. Distance equals 0 is the coast with positive (negative) distance values indicating locations over land (ocean).

diurnal amplitude is stronger (weaker) over the land (ocean) compared to the CMORPH data. Comparing Figs. 3b and 3d, the propagation speeds over land and ocean from the Du model data are similar to those from the

CMORPH data though the time phase of rainfall maximum from Du model data is 1–2 h in advance of that from the CMORPH data. A possible reason is that the rainfall derived from satellite data is always delayed by 1–2 h,

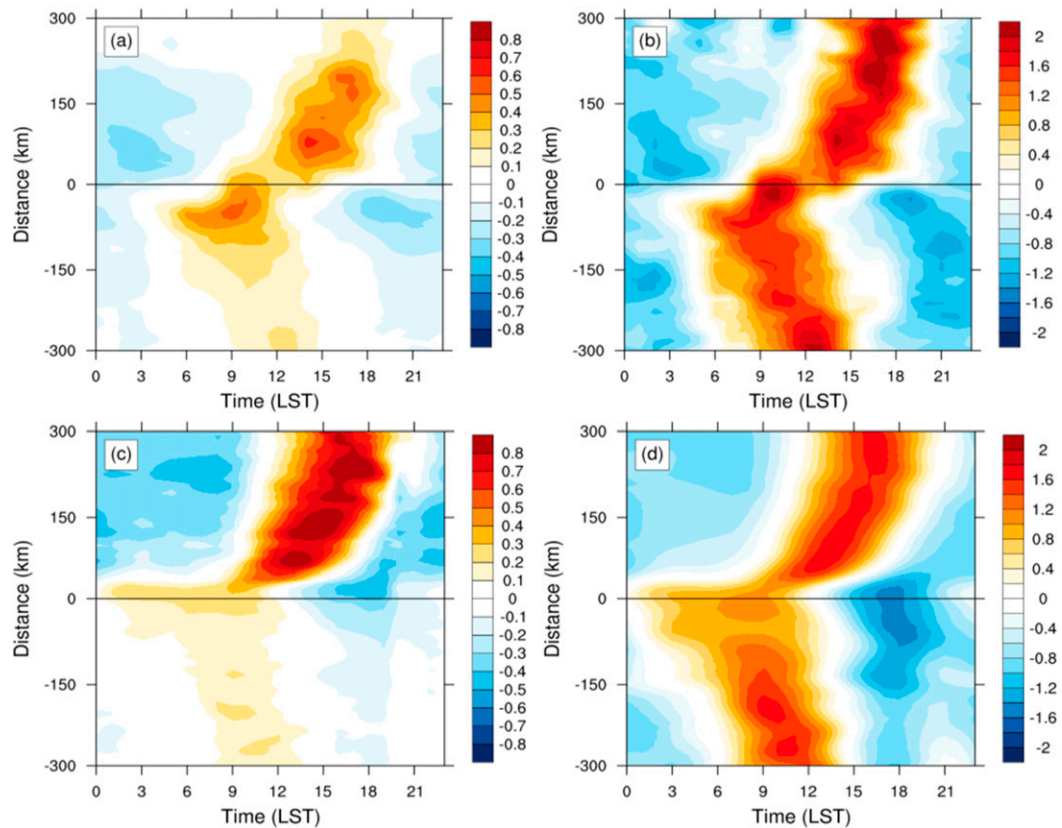


FIG. 3. Distance (latitude)-time Hovmöller diagrams of (a),(c) hourly precipitation deviations (mm) and (b),(d) normalized hourly precipitation deviations during June from 2006 to 2011 averaged over the black boxes in Fig. 1 from (a),(b) the CMORPH data and (c),(d) the Du model data.

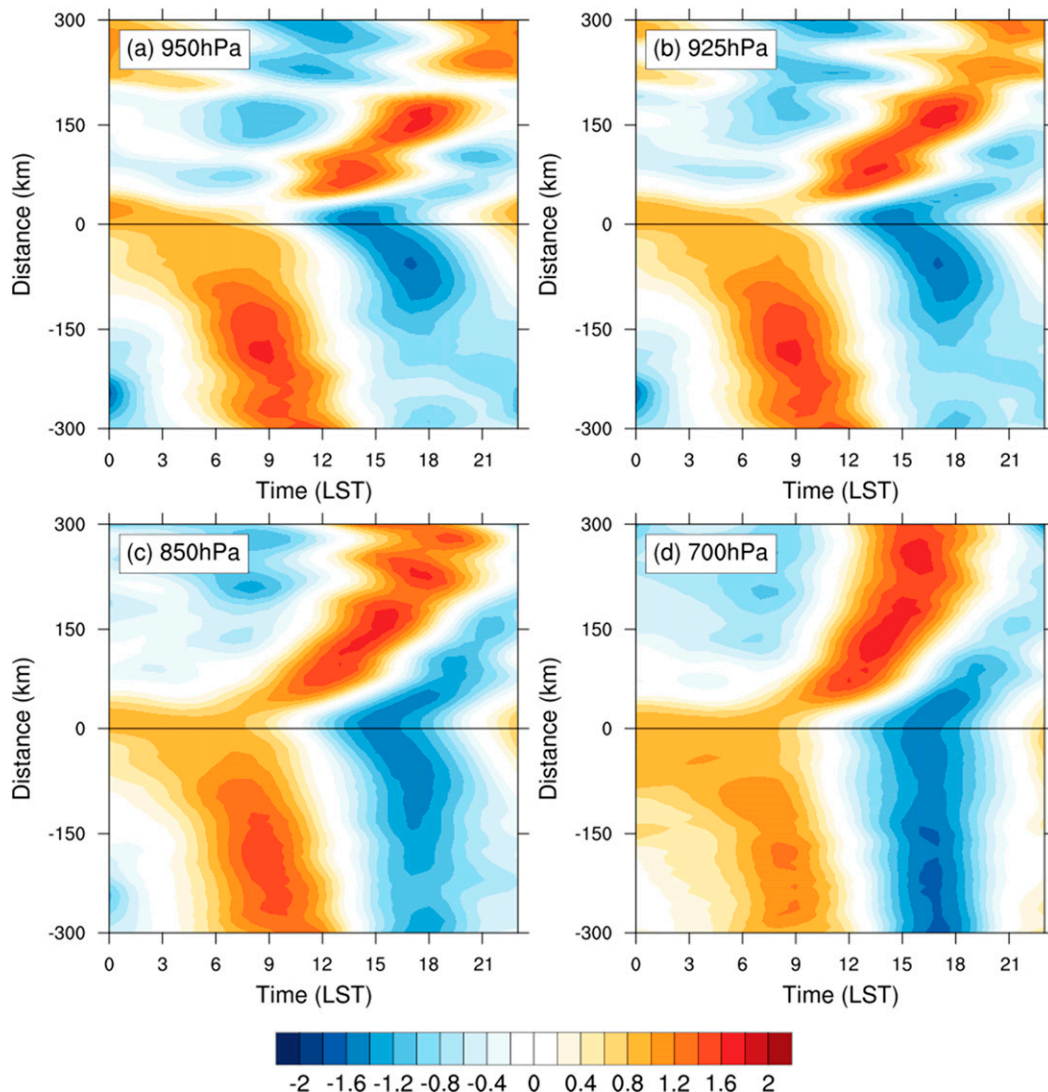


FIG. 4. Distance (latitude)–time Hovmöller diagrams of normalized hourly vertical velocity deviations at (a) 950, (b) 925, (c) 850, and (d) 700 hPa during June from 2006 to 2011, averaged over the black boxes in Fig. 1 from the Du model data.

compared to the surface observations (Chen et al. 2018). Therefore, the Du model data can well capture the diurnal rainfall propagation near the south coast of China, and they make it possible to study the mechanisms of the diurnal rainfall features.

First, the diurnal cycles of vertical velocity at different levels are analyzed. Figure 4 shows the Hovmöller diagrams of normalized vertical velocity deviations averaged over the black box (Fig. 1) from the Du model data. Similarly, the normalized vertical velocity deviation $[(w_t - \bar{w})/\sigma]$ is estimated as the vertical velocity at the current hour minus the mean vertical velocity throughout the day, normalized by the standard deviation of vertical velocity at each point.

In general, the propagation of the vertical velocity (especially at 700 hPa) is similar to that of the rainfall over both the land and the ocean (cf. Figs. 3d, 4), although the phase of the vertical velocity is 1–2 h earlier than that of the rainfall. The time lag might be because the condensation of water and fallout to the surface takes some time. Kilpatrick et al. (2017) found that the observational surface-wind-convergence maximum leads the rainfall maximum by 1–2 h in the western part of the Bay of Bengal. It is noted that the propagation of the vertical velocity over the land at different levels is different. The inland propagation speed at low levels (7–9 m s^{-1} ; Figs. 4a,b) is lower than that at midlevels (12–20 m s^{-1} ; Figs. 4c,d). Low-level (950 and 925 hPa) vertical motion over land has

some fluctuations, which might be related to terrain because local terrain might lead to small-scale thermal circulations and modulate the diurnal phase and amplitude. The difference in the propagation speed over the ocean at different levels is small (around 14–16 m s⁻¹). Based on the results from the 2D linear land–sea breeze model (Du and Rotunno 2015), the propagation pattern over the land and the ocean should be symmetric but with opposite phase. However, the diurnal propagation of winds over the land and ocean is asymmetric (Fig. 4), which we believe might be due to the effect of a background wind. A 2D linear land–sea breeze model with a background wind will be discussed in detail in section 4. Before that, the water budget will be discussed to analyze the relation between diurnal winds and diurnal rainfall from the Du model data.

c. Analysis of the rainfall budget

Following Gao et al. (2005) and Cui and Li (2006), the surface rainfall equation is derived to study the role of water vapor and cloud sources/sinks in producing the surface rainfall,

$$P = Q_{\text{WVT}} + Q_{\text{WVF}} + Q_{\text{WVE}} + Q_{\text{CM}}. \quad (3.1)$$

The surface rain rate P is contributed to by the local vapor change Q_{WVT} , vapor convergence Q_{WVF} , surface evaporation Q_{WVE} , and cloud sources/sinks Q_{CM} . The Q_{WVT} , Q_{WVF} , Q_{WVE} , and Q_{CM} can be expressed as follows:

$$Q_{\text{WVT}} = -\frac{\partial[q_v]}{\partial t} \quad (3.2)$$

$$Q_{\text{WVF}} = -\left[u \frac{\partial q_v}{\partial x}\right] - \left[v \frac{\partial q_v}{\partial y}\right] - \left[w \frac{\partial q_v}{\partial z}\right] \quad (3.3)$$

$$Q_{\text{WVE}} = E_S, \quad \text{and} \quad (3.4)$$

$$Q_{\text{CM}} = -\frac{\partial[q_l]}{\partial t} - \left[u \frac{\partial q_l}{\partial x}\right] - \left[w \frac{\partial q_l}{\partial z}\right]. \quad (3.5)$$

The variable q_v is the mixing ratio of water vapor; u and v are the components of the horizontal velocity in the x and y directions, respectively; w is the vertical velocity; and q_l is the sum of the mixing ratios of cloud water, rainwater, ice water, snow water, and graupel water. Term E_S is the surface evaporation flux. Here $[F]$ represents the mass integration $\int_0^\infty \bar{\rho} F dz$.

Figure 5 shows the Hovmöller diagrams of hourly deviations of Q_{WVT} , Q_{WVF} , Q_{CM} , Q_{WVE} , vertically integrated vertical vapor advection $-\left[w(\partial q_v/\partial z)\right]$, and P during June from 2006 to 2011 averaged over the black box in Fig. 1 from the Du model data. The diurnal propagation pattern of P (Fig. 5f) diagnosed from Eq. (3.1) is very similar to that of rainfall from the direct output of the Du model data (Fig. 3c).

The diurnal cycle of Q_{WVF} greatly contributes to the diurnal cycle of rainfall (Figs. 5b,f). The diurnal phase of Q_{WVT} is nearly opposite of that of Q_{WVF} . The diurnal cycle Q_{CM} is not significant (Fig. 5c). Surface evaporation over the land exhibits an obvious diurnal cycle with a maximum near noon (1300LST) that partly contributes to afternoon the peak over the land, whereas the diurnal cycle of surface evaporation over the ocean is very weak (Fig. 5d). For the vapor convergence, vertically integrated vertical vapor advection is the main contributor (Fig. 5e). Comparing Figs. 4c and 4d with Fig. 5b, the diurnal cycle of vertical velocity at midlevels is similar to that of the vapor convergence; thus, the midlevels (around 850–700 hPa) appear to be the key levels, since both the moisture and vertical velocity at the midlevels are significant. Therefore, the diurnal cycle of rainfall is closely associated with that of the vertical velocity at these levels.

4. Linear land–sea breeze theory with a background wind

a. Linear equations and analytical solutions

The 2D linear equations of motion under the Boussinesq and hydrostatic approximations with a background wind can be written as (Rotunno 1983; Qian et al. 2009; Du and Rotunno 2015)

$$\left(\frac{\partial}{\partial t} + V \frac{\partial}{\partial y}\right)u - fv = 0 \quad (4.1)$$

$$\left(\frac{\partial}{\partial t} + V \frac{\partial}{\partial y}\right)v + fu = -\frac{\partial \phi}{\partial y} \quad (4.2)$$

$$-b = -\frac{\partial \phi}{\partial z} \quad (4.3)$$

$$\left(\frac{\partial}{\partial t} + V \frac{\partial}{\partial y}\right)b + N^2 w = Q_0 \left[\frac{\pi}{2} + \tan^{-1}\left(\frac{y}{y_0}\right)\right] e^{-z/z_0} e^{-i\omega t}, \quad (4.4)$$

and

$$\frac{\partial v}{\partial y} + \frac{\partial w}{\partial z} = 0, \quad (4.5)$$

where V is background wind in the y direction; (u, v, w) are the wind components in the (x, y, z) directions, respectively; ϕ is the geopotential height; b is the buoyancy; and N^2 is the static stability. The heating function is $Q_0[(\pi/2) + \tan^{-1}(y/y_0)]e^{-z/z_0}e^{-i\omega t}$, where the horizontal scale of the land–sea contrast in heating is denoted by y_0 and the vertical scale of the heating is denoted by z_0 . The quantity ω equals $2\pi \text{ day}^{-1}$, Q_0 is the maximum heating rate, and $t = 0$ corresponds to noon. The coastline is at $y = 0$ with land to the north ($y > 0$) and ocean to the south. The heating and the motion are taken to be independent of x .

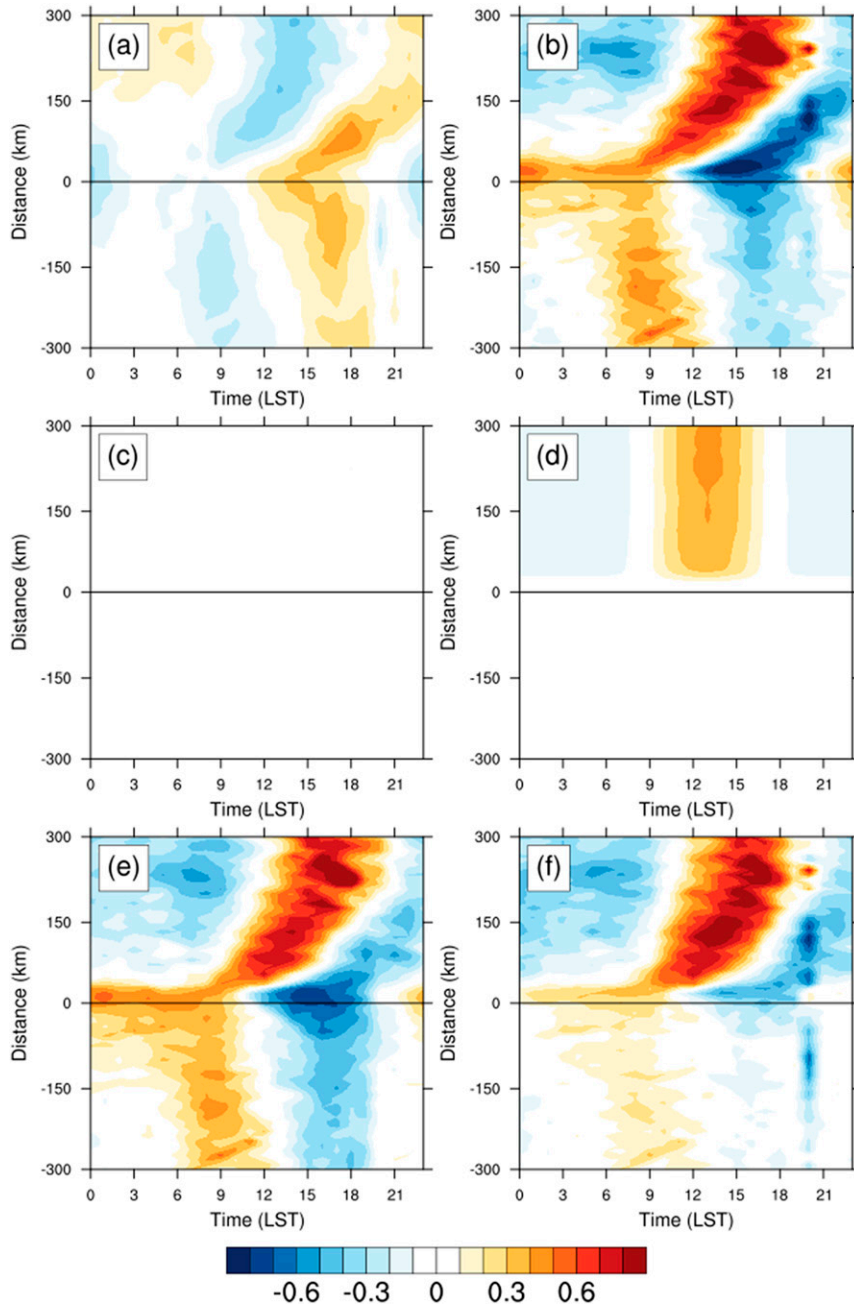


FIG. 5. Distance (latitude)–time Hovmöller diagrams of hourly deviations of (a) Q_{WVT} , (b) Q_{WVF} , (c) Q_{CM} , (d) Q_{WVE} , (e) $-[w(\partial q_v/\partial z)]$, and (f) $P = Q_{WVT} + Q_{WVF} + Q_{WVE} + Q_{CM}$ (mm) during June from 2006 to 2011, averaged (at constant distance) across the black boxes in Fig. 1 from the Du model data.

Combining Eqs. (4.1)–(4.5) into a single equation for the streamfunction ψ with $v = \partial\psi/\partial z$ and $w = -\partial\psi/\partial y$ we find

$$N^2 \frac{\partial^2 \psi}{\partial y^2} + \left[f^2 + \left(\frac{\partial}{\partial t} + V \frac{\partial}{\partial y} \right)^2 \right] \frac{\partial^2 \psi}{\partial z^2} = -\frac{\partial Q}{\partial y} = -Q_0 \left(\frac{y_0}{y_0^2 + y^2} \right) e^{-z/z_0} e^{-i\omega t}. \tag{4.6}$$

It is assumed that $\psi = \text{Re}[\Psi(y, z)e^{-i\omega t}]$; substituting this into Eq. (4.6) then gives

$$N^2 \frac{\partial^2 \Psi}{\partial y^2} + \left[f^2 + \left(-i\omega + V \frac{\partial}{\partial y} \right)^2 \right] \frac{\partial^2 \Psi}{\partial z^2} = -Q_0 \left(\frac{y_0}{y_0^2 + y^2} \right) e^{-z/z_0}. \tag{4.7}$$

The Fourier transform of Eq. (4.7) in the y direction becomes

$$-N^2 K^2 \hat{\psi} + (f^2 - \sigma^2) \frac{\partial^2 \hat{\psi}}{\partial z^2} = -Q_0 \sqrt{\frac{\pi}{2}} e^{-y_0 |K|} e^{-z/z_0}, \quad (4.8)$$

where K is the nondimensional horizontal wavenumber, $\sigma = \omega - KV$, and $\hat{\psi} = \int_{-\infty}^{\infty} \psi e^{-iKy} dy$.

Considering $V > 0$ and $f < \omega$ (latitude is less than 30°N) and boundary conditions $\hat{\psi} = 0$ when $z = 0$ and $\hat{\psi}$ is finite and/or satisfies the radiation condition when $z = \infty$, the solution of Eq. (4.8) is

$$\hat{\psi} = \begin{cases} T \left\{ e^{-z/z_0} - e^{-i\sqrt{[N^2 K^2 / (\sigma^2 - f^2)]z}} \right\} & \text{when } K < \frac{\omega - f}{V} \\ T \left\{ e^{-z/z_0} - e^{-\sqrt{[N^2 K^2 / (f^2 - \sigma^2)]z}} \right\} & \text{when } \frac{\omega - f}{V} < K < \frac{\omega + f}{V}, \\ T \left\{ e^{-z/z_0} - e^{i\sqrt{[N^2 K^2 / (\sigma^2 - f^2)]z}} \right\} & \text{when } K > \frac{\omega + f}{V} \end{cases}, \quad (4.9)$$

where

$$T = -\sqrt{\frac{\pi}{2}} \frac{Q_0}{[(f^2 - \sigma^2)/z_0^2] - N^2 K^2} e^{-y_0 |K|}.$$

Applying the inverse Fourier transform $\psi = \text{Re}[(1/2\pi) \int_{-\infty}^{\infty} \hat{\psi} e^{i(Ky - \omega t)} dK]$, we obtain

$$w = -\frac{\partial \psi}{\partial y} = I_1 + I_2 + I_3, \quad (4.10)$$

where

$$\begin{aligned} I_1 &= \text{Re} \left(\frac{1}{2\pi} \int_{-\infty}^{(\omega - f)/V} (-iK) T \left\{ e^{-z/z_0} - e^{-i\sqrt{[N^2 K^2 / (\sigma^2 - f^2)]z}} \right\} dK \right) \\ I_2 &= \text{Re} \left(\frac{1}{2\pi} \int_{(\omega - f)/V}^{(\omega + f)/V} (-iK) T \left\{ e^{-z/z_0} - e^{-\sqrt{[N^2 K^2 / (f^2 - \sigma^2)]z}} \right\} dK \right) \\ I_3 &= \text{Re} \left(\frac{1}{2\pi} \int_{(\omega + f)/V}^{\infty} (-iK) T \left\{ e^{-z/z_0} - e^{i\sqrt{[N^2 K^2 / (\sigma^2 - f^2)]z}} \right\} dK \right). \end{aligned}$$

In this study these integrations are calculated numerically using MATLAB.

When $V = 0$, only I_1 is nonzero, which is same as the solution in [Du and Rotunno \(2015\)](#) without a background wind. When $f = 0$, $I_2 = 0$, and we recover the solution of [Qian et al. \(2009\)](#); note that the present I_1 includes their I_1 and I_2 .

b. Land–sea circulations with and without a background wind

First, we set $f = 4.79 \times 10^{-5} \text{ s}^{-1}$ (20°N), which is near the south coast of China, $Q_0 = 1.2 \times 10^{-5} \text{ m s}^{-3}$, $z_0 = 1 \text{ km}$, $N = 0.01 \text{ s}^{-1}$, and $y_0 = 50 \text{ km}$ in Eq. (4.10) and obtain the diurnal cycle of the vertical velocity in the y – z

plane with $V = 0$ ([Fig. 6](#)), 3 ([Fig. 7](#)), and 5 m s^{-1} ([Fig. 8](#)). Note that $y > 0$ is the land side.

[Figure 6](#) shows the y – z cross section of vertical velocity over a diurnal cycle at 20°N from the 2D linear model when $V = 0$. The land–sea circulation is symmetric with opposite phase and has wavelike features as the situation (latitude less than 30°N) in [Du and Rotunno \(2015\)](#).

With increasing background wind ($V > 0$), the phase lines and ray paths are more steeply inclined to the vertical over the ocean ($y < 0$), and the phase lines and ray paths are less steeply inclined over the land ([Figs. 7, 8](#)). [Figure 9](#) shows y – z cross sections of vertical velocity and their three contributors (I_1 , I_2 , and I_3) over a diurnal cycle with

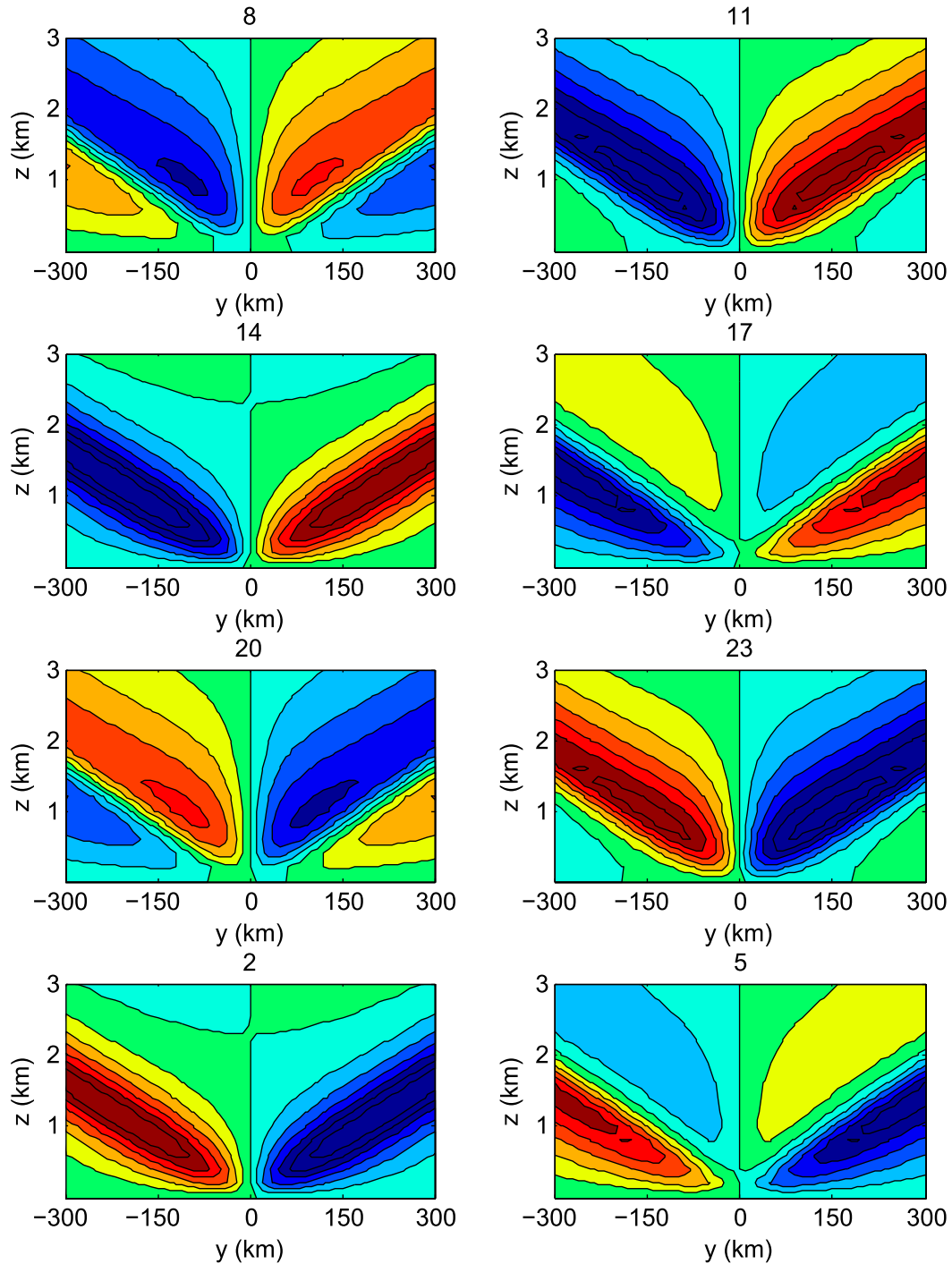


FIG. 6. The y - z structure of the vertical velocity over a diurnal cycle at 0800, 1100, 1400, 1700, 2000, 2300, 0200, and 0500 LST from the linear model without background wind. Positive (warm colors) and negative (cold colors) values are indicated.

background wind (5 m s^{-1}). Northward-propagating waves with negative phase tilts exist over the land with larger V (Fig. 9), which is related to I_3 . Qian et al. (2009) indicate that I_3 is broadly similar to flow past a

stationary heat source or topographic obstacle. The contributions from I_1 correspond to the two contributions (their I_1 and I_2) described by Qian et al. (2009), including Doppler shifting and associated tilting of the

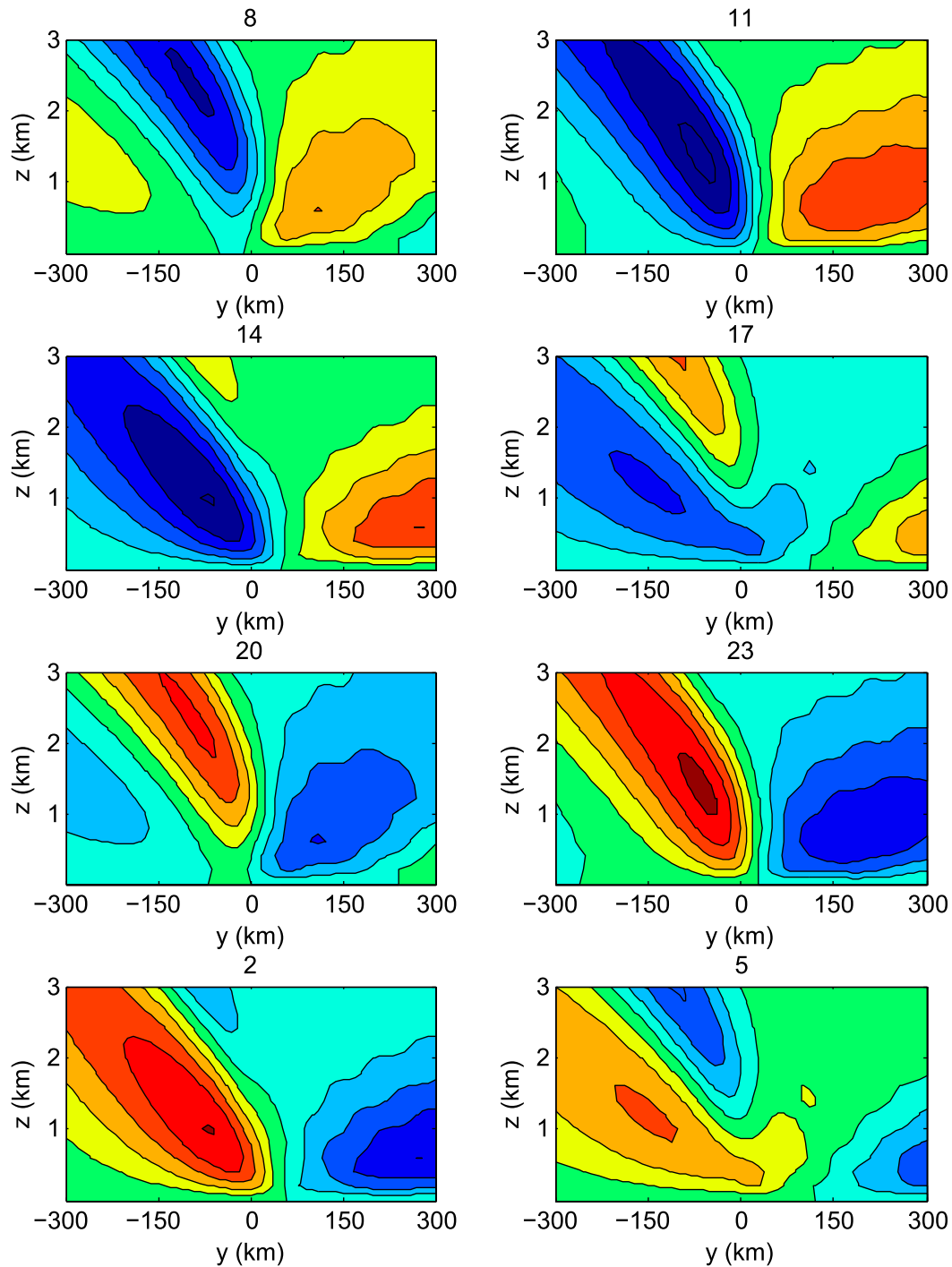


FIG. 7. As in Fig. 6, but with a background wind of 3 m s^{-1} .

ray paths, whose tilt is controlled by the background wind. The contribution from I_2 is related to the Coriolis force, which does not exist in the solution for $f = 0$ (Qian et al. 2009). The contribution from I_2 represents

the advection effect of the background wind on vertically trapped circulations. The horizontal speed of the wave calculated from Fig. 9 (third column) corresponds to the background wind speed.

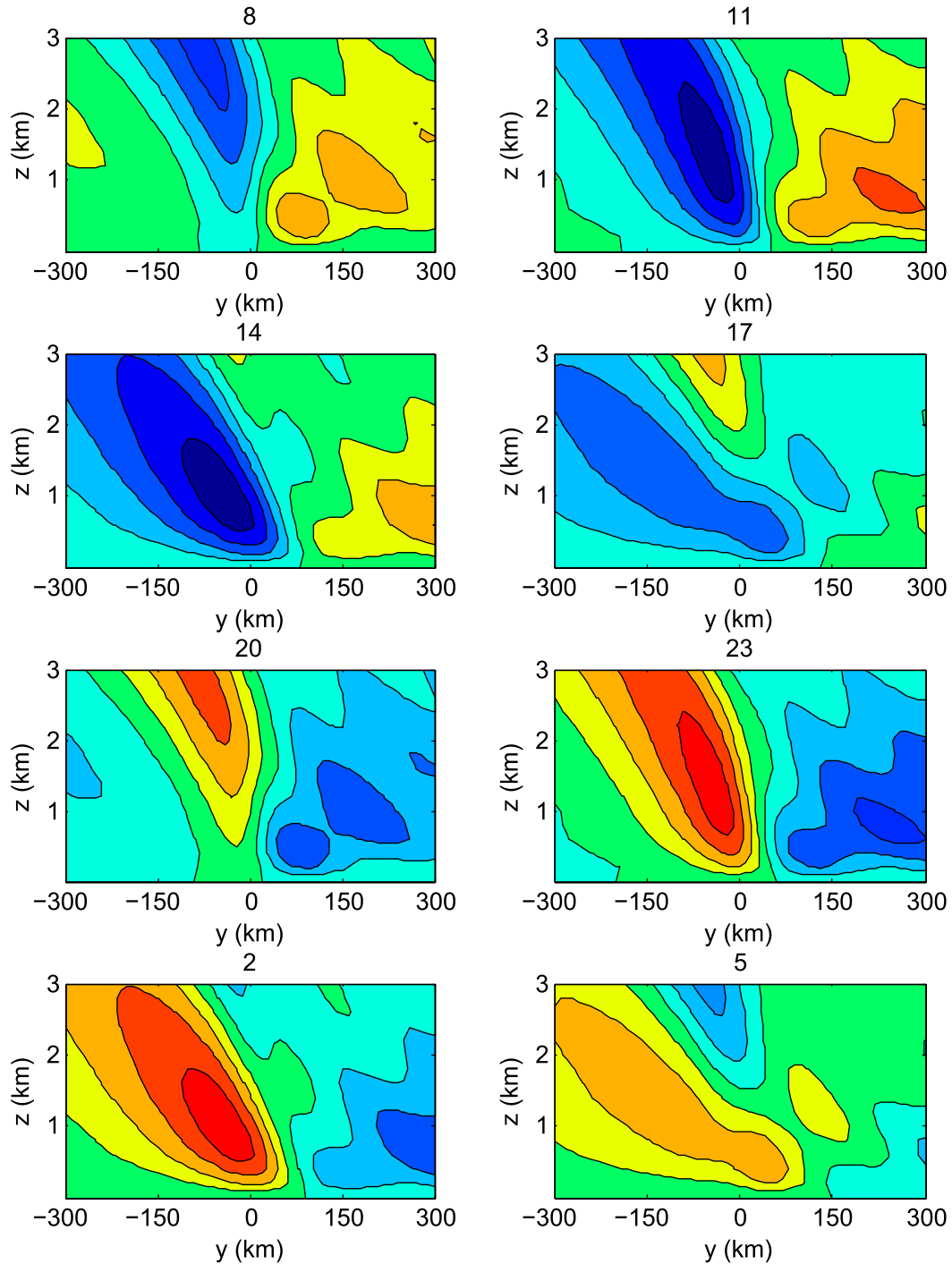


FIG. 8. As in Fig. 6, but with a background wind of 5 m s^{-1} .

Figure 10 shows Hovmöller diagrams of hourly vertical velocity deviations at different levels with and without background wind from the 2D linear land–sea breeze model. Without a background wind, the propagation pattern is symmetric with opposite

phases with respect to the coastline at different levels (Figs. 10a,b). The pattern becomes asymmetric with respect to the coastline with a background wind (Figs. 10c,d). Over the land, the propagation speed at low levels (950 hPa; Fig. 10c) is slower than that at

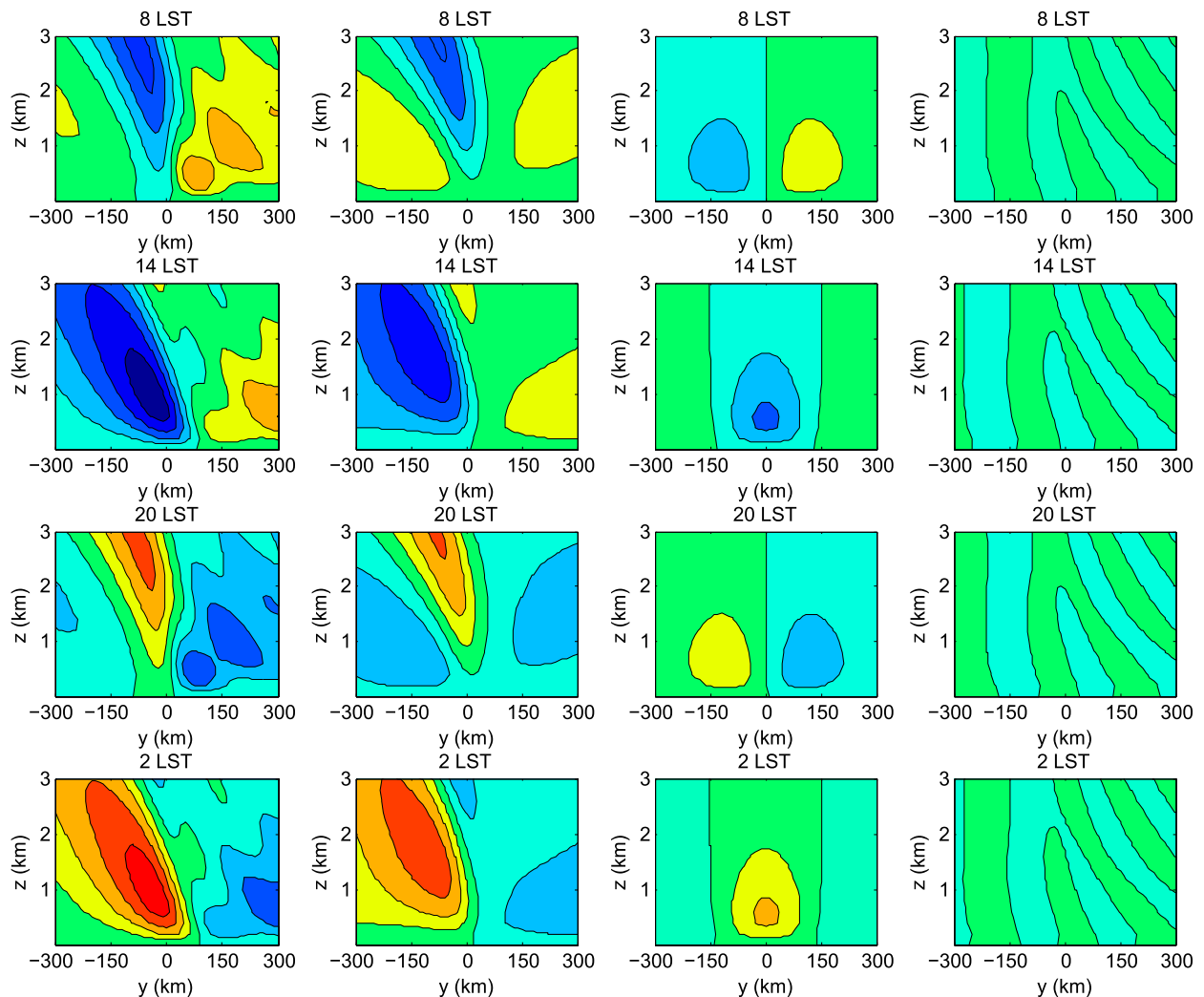


FIG. 9. The y - z structure of (first column) the vertical velocity, (second column) the I_1 term, (third column) the I_2 term, and (fourth column) the I_3 term of Eq. (4.10) over a diurnal cycle at 0800, 1400, 2000, and 0200 LST from the linear model with a background wind of 5 m s^{-1} . Positive (warm colors) and negative (cold colors) values are indicated.

midlevel (850 hPa;¹ Fig. 10d), which is similar to the results from the Du model data. It is noted that discrepancies exist between the linear model and the Du model data as result of the absence of many factors (terrain, boundary layer effects, moisture, etc.). However, the important point is that the linear model with a background wind is much closer to the Du model data than is the linear model without a background wind. At low levels, both I_1 and I_2 are the main components for the propagation mode, whereas I_1 is more significant at higher levels. When the background wind is large, I_3 becomes important over the

land and modulates the propagation pattern with negative tilts.

Therefore, the background wind plays a significant role in the diurnal propagation of winds based on the results from the present 2D linear model and the Du model data, which are consistent. To further verify the effect of background wind, WRF idealized simulations are presented in the next section.

5. Idealized simulations

a. Configuration of the idealized WRF Model

Following the configuration from Du and Rotunno (2015), we simulate an idealized sea breeze with the 2D version of WRF ARW (Skamarock and Klemp 2008). The simulation covers 3000 km in the y

¹ Because of the absence of moist process in the linear model, the maximum vertical motion occurs around 850 hPa rather than 700 hPa as in the Du model data.

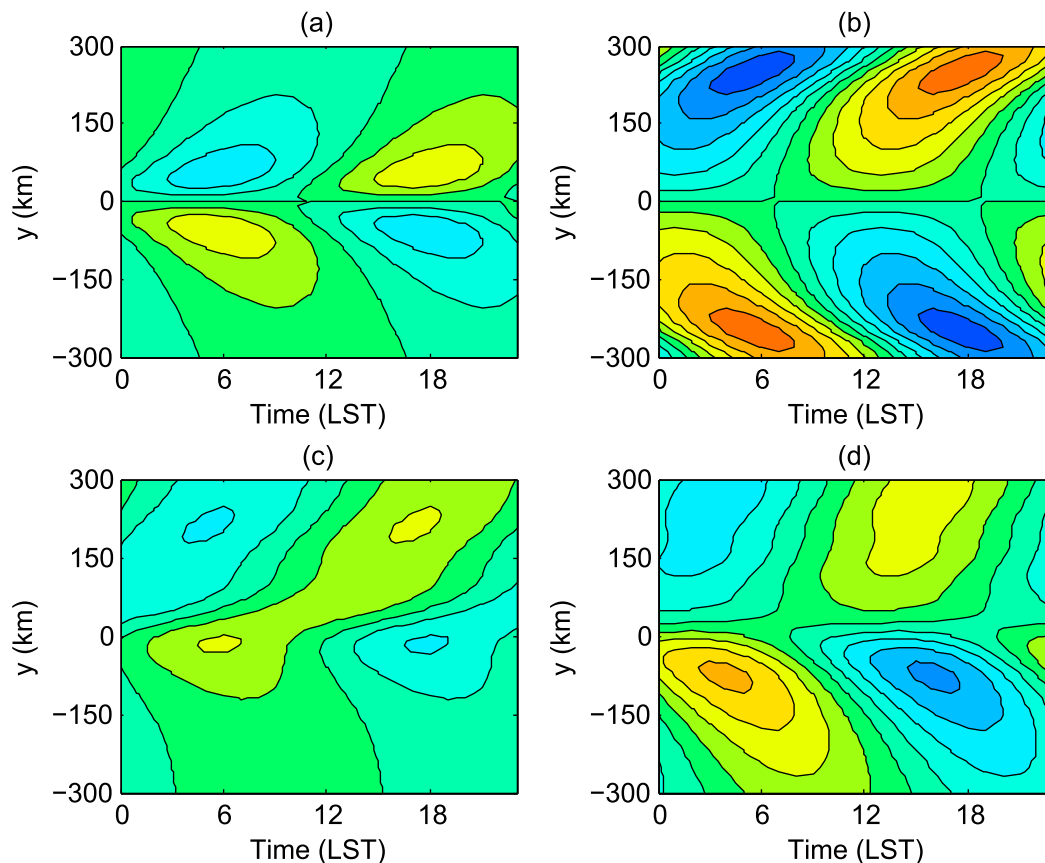


FIG. 10. Distance (latitude)–time Hovmöller diagrams of hourly vertical velocity deviations at (a),(c) 950 and (b),(d) 850 hPa from the 2D linear land–sea breeze model (a),(b) without and (c),(d) with a background wind ($V = 3 \text{ m s}^{-1}$). The location $y > 0$ is over the land and $y < 0$ is over the ocean.

direction with land in the middle spanning 1000 km and ocean on either side. The purpose of the idealized experiments is to check that the idealized model can obtain similar results to the linear theory; thus, we set the amplitude of the diurnal heat flux over the land and the vertical diffusion coefficient for heat to the relatively small value of 20 W m^{-2} and $6 \text{ m}^2 \text{ s}^{-1}$, respectively [experiments 1 and 2 (EXP1 and EXP2), respectively]. Then through setting more realistic values of the heat flux and the vertical diffusion coefficient (EXP3 and EXP4), we can further check the effects of certain nonlinear processes. The detailed description of the configuration is in section 4a of Du and Rotunno (2015), and EXP1–4 in Table 1 in this study.

b. Simulations with and without background wind

Figures 11a and 11b show Hovmöller diagrams of the vertical velocity deviation at 950 and 850 hPa, respectively, with no background wind. The propagation pattern at the lower level is similar to the case at 25°N in

Du and Rotunno (2015, their Figs. 9c, 10c). The propagation at the higher level has a similar propagation speed to that at the lower level but with a different time phase and a different location of the maximum. The propagation over the land and ocean is symmetric with opposite phase as expected in the 2D linear theory discussed in section 5.

Figures 11c and 11d are as in Figs. 11a and 11b, but with an onshore background wind (3 m s^{-1}). Comparing Figs. 11c and 11d and Figs. 10c and 10d, these asymmetric patterns are similar and thus they further verify the effect of the background wind from the 2D linear theory. The idealized model has a 1–2-h phase lag with respect to the 2D linear theory because the vertical transport of heat from the surface takes time in the idealized model, whereas the atmosphere is heated simultaneously in the whole column in the 2D linear theory (Du and Rotunno 2015). The phase lag in the idealized WRF Model brings the absolute time phase closer to that from the Du model data as compared to that from the 2D linear model.

TABLE 1. WRF Model and physics settings used for the experiments.

WRF settings	Value			
	EXP1	EXP2	EXP3	EXP4
Background wind (m s^{-1})	0	3	0	5
Coriolis parameter (10^{-4} s^{-1})			0.479	
Vertical diffusion for momentum ($\text{m}^2 \text{ s}^{-1}$)	0		60	
Horizontal diffusion for momentum and heat ($\text{m}^2 \text{ s}^{-1}$)		0		
Vertical diffusion for heat ($\text{m}^2 \text{ s}^{-1}$)	6		60	
Drag coefficient		0		
Heat flux over land (W m^{-2})	20 $\cos\omega t$, where ω is diurnal frequency; starting time is 1300 LST		100 $\cos\omega t$, where ω is diurnal frequency; starting time is 1300 LST	
Heat flux over ocean (W m^{-2})		0		
Moisture flux [$\text{g m} (\text{kg s})^{-1}$]		0		
Horizontal grid spacing (km)		5		
Vertical levels		40		
Longwave physics		None		
Shortwave physics		None		
Surface scheme		Thermal diffusion scheme		
Surface-layer scheme		None		
Cumulus scheme		None		
Microphysics scheme		None		
Initial wind (m s^{-1})		0		
Initial lapse rate of potential temperature (K km^{-1})		5		

When we set a more realistic value for the amplitude of the diurnal heat flux over the land (100 W m^{-2}), the vertical diffusion coefficient for heat ($60 \text{ m}^2 \text{ s}^{-1}$), and background wind (5 m s^{-1}), the results with respect to the effect of background wind are shown in Fig. 12 (see EXP3 and EXP4 in Table 1 for detailed configurations). Similarly, the propagation over the land and ocean also becomes asymmetric under the effect of background wind, though the speed and phase of the propagation is different from those in the linear situation (Fig. 11). Since many other factors (e.g., terrain, cold pools, moisture effects, boundary layer processes) are not included in the idealized 2D model, the discrepancies between the idealized WRF simulation with a background wind (Fig. 12) and the Du model data (Fig. 4) exist in terms of propagation speed and the diurnal phase and amplitude. It is noted that the diurnal signals over the ocean from the idealized WRF simulations are much stronger than that from the Du model data and the CMORPH observations, which might be because marine boundary layer processes are not included in the idealized WRF simulations.

6. Summary and discussion

A diurnal cycle of rainfall occurs globally and its propagation near the coast over the tropics has been

observed and studied extensively. In this study, we utilized the Climate Prediction Center morphing technique (CMORPH rainfall data, 8-km horizontal resolution, and 30-min temporal resolution; June 1998–2005) to study the diurnal cycle of rainfall near the south coast of China. The CMORPH data indicate that the rainfall peak over the ocean occurs in the morning with offshore (southward) propagation, whereas rainfall over the land reaches a maximum in the afternoon with onshore (northward) propagation.

Long-term (June 2006–11) hourly high-resolution model data (9-km horizontal resolution and 40 vertical levels) simulated with a mesoscale model (WRF) from the 12- to 36-h simulation of each day (Du et al. 2014; Du model data) can well capture the propagation features of diurnal rainfall. It is found that the diurnal propagation of vertical velocity is broadly similar to that of rainfall though there are different propagation speeds at different levels over land. Through diagnosing the rainfall rate from the rainfall budget, we found that the diurnal cycle of vertically integrated vertical vapor advection is the main contributor to the diurnal cycle of rainfall, and therefore the diurnal cycle of vertical velocity at midlevels is a good indicator for the diurnal cycle of rainfall.

The present linear land–sea breeze model indicates that background wind is a key factor for the offshore and

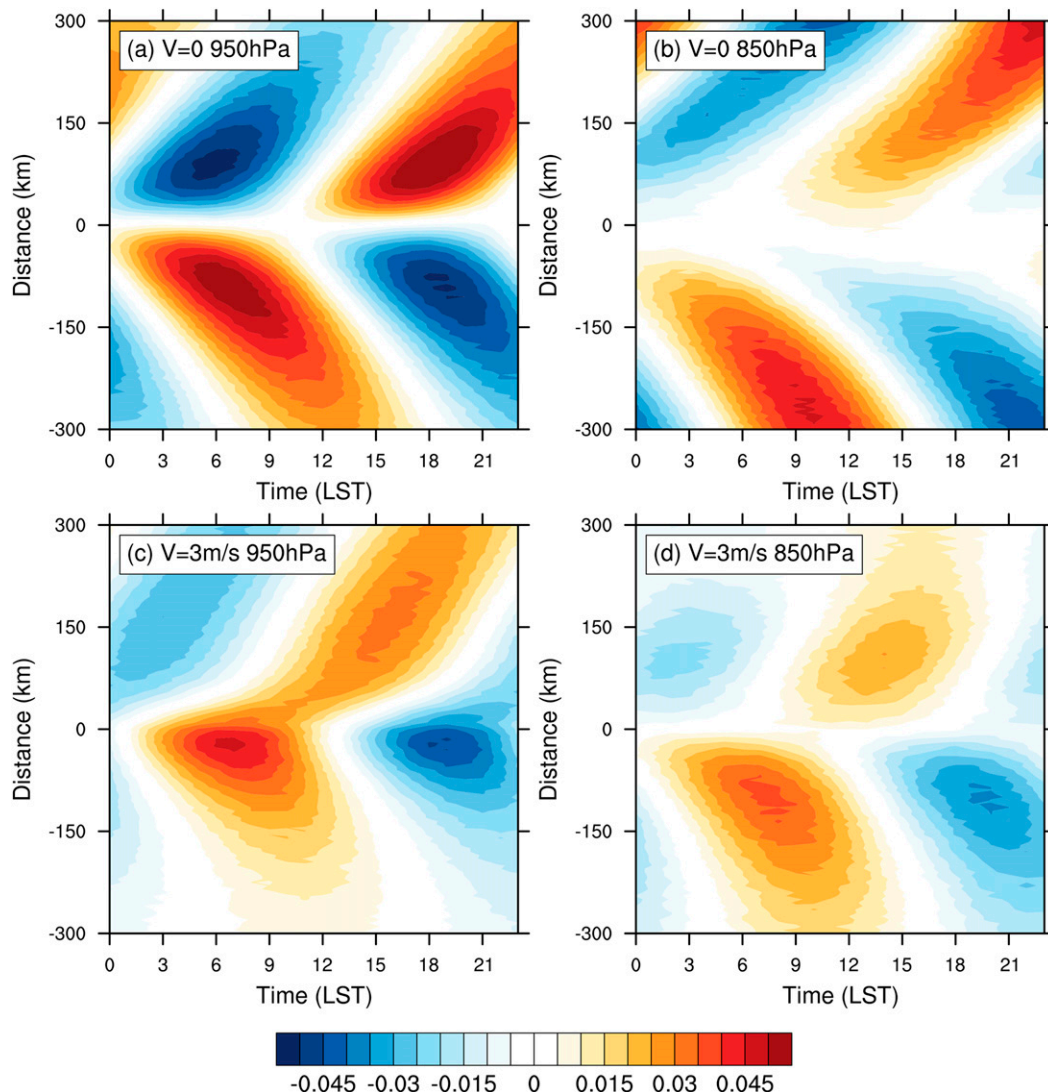


FIG. 11. As in Fig. 10, but from the WRF 2D idealized model experiments (EXP1 and EXP2).

onshore propagation pattern near the coast. Without the background wind, the two-way propagation exists and is symmetric with opposite phases, which is the classical inertia-gravity wave response to land-sea thermal forcing (Rotunno 1983, Du and Rotunno 2015). The background wind can change the propagation pattern. With increasing background wind, the degree of propagation asymmetry with respect to the coastline is more in agreement with the Du model data. The background wind changes the tilt of the ray paths via contribution I_1 [Eq. (4.10)] in the analytical solution, which is associated with Doppler shifting. The background wind may also introduce an overland (north side) wave response with negative tilts over the land via the term I_3 , which is similar to flow past a

stationary heat source or a topographic obstacle. The term I_2 indicates that the background wind has the effect of advection of trapped disturbances. The idealized land-sea breeze model using a simplified version of WRF also was able to capture the propagation signals near the coast and the effect of background wind.

This paper focuses on one possible mechanism of diurnal propagation: inertia-gravity waves triggered by the diurnal land-sea thermal contrast. The rainfall diurnal propagation over the south coast of China is a phenomenon involving many scales and is related to multiple physical mechanisms. Other mechanisms such as atmospheric stability change, terrain, low-level jets, cold-pool dynamics, and urban impacts, are

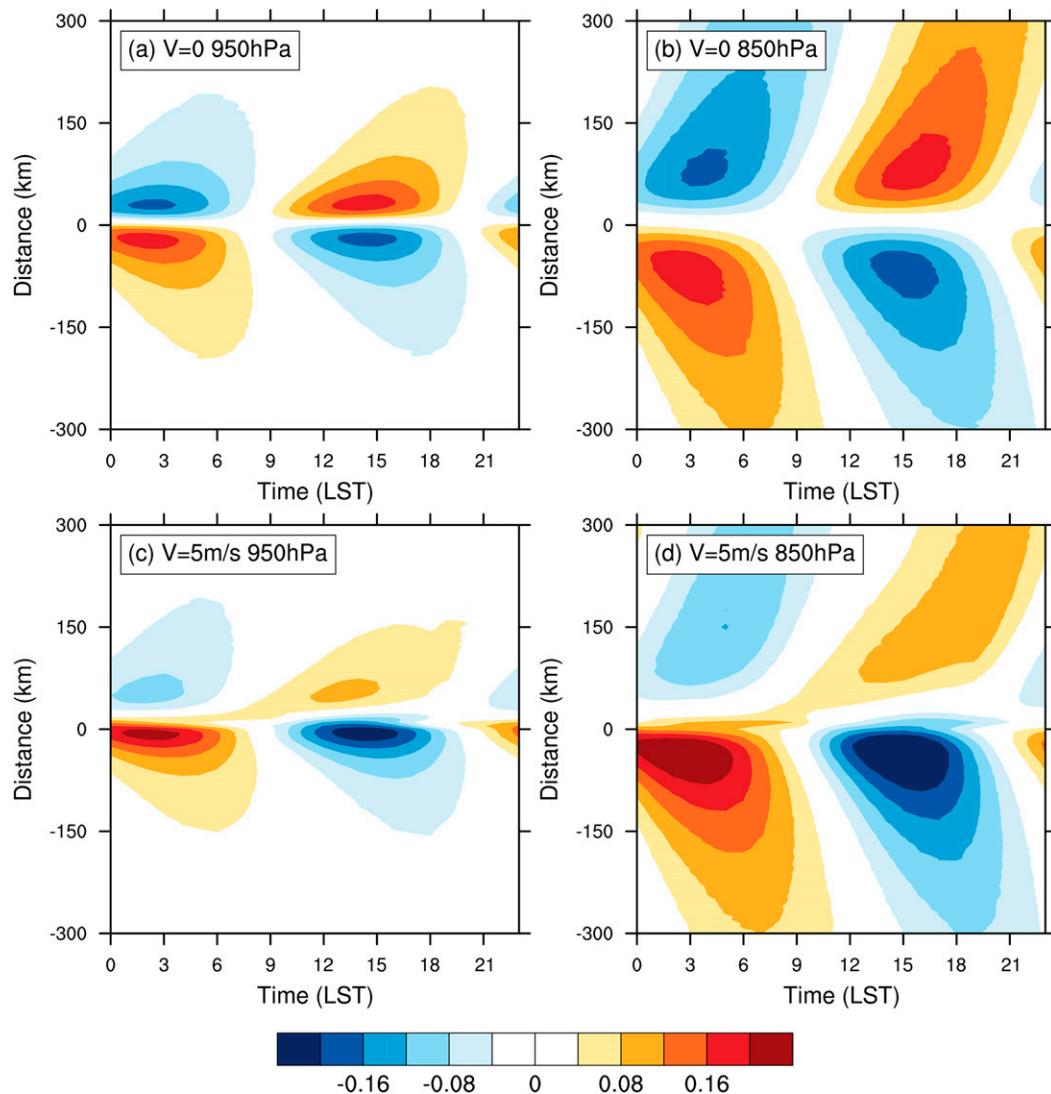


FIG. 12. As in Fig. 10, but from the WRF 2D idealized model experiments (EXP3 and EXP4).

important, but they are outside of the scope of this study and are left to future work.

Acknowledgments. This study was supported by the program “The One Hundred Talent Recruitment Program II, Sun Yat-sen University” (74110-52601118). The authors are thankful to Dr. Stanley Trier (NCAR) for his informal review, and Prof. Guixing Chen (Sun Yat-sen University, China) for the fruitful discussions.

REFERENCES

- Aves, S. L., and R. H. Johnson, 2008: The diurnal cycle of convection over the northern South China Sea. *J. Meteor. Soc. Japan*, **86**, 919–934, <https://doi.org/10.2151/jmsj.86.919>.
- Bao, X., F. Zhang, and J. Sun, 2011: Diurnal variations of warm season precipitation east of the Tibetan Plateau over China. *Mon. Wea. Rev.*, **139**, 2790–2810, <https://doi.org/10.1175/MWR-D-11-00006.1>.
- Carbone, R. E., and J. D. Tuttle, 2008: Rainfall occurrence in U.S. warm season: The diurnal cycle. *J. Climate*, **21**, 4132–4146, <https://doi.org/10.1175/2008JCLI2275.1>.
- , —, D. A. Ahijevych, and S. B. Trier, 2002: Inferences of predictability associated with warm season precipitation episodes. *J. Atmos. Sci.*, **59**, 2033–2056, [https://doi.org/10.1175/1520-0469\(2002\)059<2033:IOPAWW>2.0.CO;2](https://doi.org/10.1175/1520-0469(2002)059<2033:IOPAWW>2.0.CO;2).
- Chen, G., W. Sha, and T. Iwasaki, 2009: Diurnal variation of precipitation over southeastern China: Spatial distribution and its seasonality. *J. Geophys. Res.*, **114**, D13103, <https://doi.org/10.1029/2008JD011103>.
- , —, —, and K. Ueno, 2012: Diurnal variation of rainfall in the Yangtze River Valley during the spring–summer transition from TRMM measurements. *J. Geophys. Res.*, **117**, D06106, <https://doi.org/10.1029/2011JD017056>.
- , —, M. Sawada, and T. Iwasaki, 2013: Influence of summer monsoon diurnal cycle on moisture transport and precipitation

- over eastern China. *J. Geophys. Res. Atmos.*, **118**, 3163–3177, <https://doi.org/10.1002/jgrd.50337>.
- , R. Lan, W. Zeng, H. Pan, and W. Li, 2018: Diurnal variations of rainfall in surface and satellite observations at a summer monsoon. *J. Climate*, **31**, 1703–1724, <https://doi.org/10.1175/JCLI-D-17-0373.1>.
- Chen, X., K. Zhao, M. Xue, B. Zhou, X. Huang, and W. Xu, 2015: Radar-observed diurnal cycle and propagation of convection over the Pearl River Delta during Mei-Yu season. *J. Geophys. Res.*, **120**, 12 557–12 575, <https://doi.org/10.1002/2015JD023872>.
- , F. Zhang, and K. Zhao, 2016: Diurnal variations of the land–sea breeze and its related precipitation over south China. *J. Atmos. Sci.*, **73**, 4793–4815, <https://doi.org/10.1175/JAS-D-16-0106.1>.
- , —, and —, 2017: Influence of monsoonal wind speed and moisture content on intensity and diurnal variations of the mei-yu season coastal rainfall over south China. *J. Atmos. Sci.*, **74**, 2835–2856, <https://doi.org/10.1175/JAS-D-17-0081.1>.
- Cui, X., and X. Li, 2006: Role of surface evaporation in surface rainfall processes. *J. Geophys. Res.*, **111**, D17112, <https://doi.org/10.1029/2005JD006876>.
- Dai, A., and C. Deser, 1999: Diurnal and semidiurnal variations in global surface wind and divergence fields. *J. Geophys. Res.*, **104**, 31 109–31 125, <https://doi.org/10.1029/1999JD900927>.
- Drobinski, P., R. Rotunno, and T. Dubos, 2011: Linear theory of the sea breeze in a thermal wind. *Quart. J. Roy. Meteor. Soc.*, **137**, 1602–1609, <https://doi.org/10.1002/qj.847>.
- Du, Y., and R. Rotunno, 2015: Thermally driven diurnally periodic wind signals off the east coast of China. *J. Atmos. Sci.*, **72**, 2806–2821, <https://doi.org/10.1175/JAS-D-14-0339.1>.
- , Q. H. Zhang, Y. L. Chen, Y. Y. Zhao, and X. Wang, 2014: Numerical simulations of spatial distributions and diurnal variations of low-level jets in China during early summer. *J. Climate*, **27**, 5747–5767, <https://doi.org/10.1175/JCLI-D-13-00571.1>.
- , R. Rotunno, and Q. Zhang, 2015a: Analysis of WRF-simulated diurnal boundary-layer winds in eastern China using a simple 1D model. *J. Atmos. Sci.*, **72**, 714–727, <https://doi.org/10.1175/JAS-D-14-0186.1>.
- , Y.-L. Chen, and Q. Zhang, 2015b: Numerical simulations of the boundary layer jet off the southeastern coast of China. *Mon. Wea. Rev.*, **143**, 1212–1231, <https://doi.org/10.1175/MWR-D-14-00348.1>.
- Gao, S., X. Cui, Y. Zhou, and X. Li, 2005: Surface rainfall processes as simulated in a cloud-resolving model. *J. Geophys. Res.*, **110**, D10202, <https://doi.org/10.1029/2004JD005467>.
- Garreaud, R. D., and R. Muñoz, 2004: The diurnal cycle in circulation and cloudiness over the subtropical southeast Pacific: A modeling study. *J. Climate*, **17**, 1699–1710, [https://doi.org/10.1175/1520-0442\(2004\)017<1699:TDCICA>2.0.CO;2](https://doi.org/10.1175/1520-0442(2004)017<1699:TDCICA>2.0.CO;2).
- Gille, S. T., S. G. Llewellyn Smith, and N. M. Stom, 2005: Global observations of the land breeze. *Geophys. Res. Lett.*, **32**, L05605, <https://doi.org/10.1029/2004GL022139>.
- Hassim, M. E. E., T. P. Lane, and W. W. Grabowski, 2016: The diurnal cycle of rainfall over New Guinea in convection-permitting WRF simulations. *Atmos. Chem. Phys.*, **16**, 161–175, <https://doi.org/10.5194/acp-16-161-2016>.
- He, H., and F. Zhang, 2010: Diurnal variations of warm-season precipitation over northern China. *Mon. Wea. Rev.*, **138**, 1017–1025, <https://doi.org/10.1175/2010MWR3356.1>.
- Houze, R. A., Jr., 2004: Mesoscale convective systems. *Rev. Geophys.*, **42**, RG4003, <https://doi.org/10.1029/2004RG000150>.
- Jiang, Q., 2012a: On offshore propagating diurnal waves. *J. Atmos. Sci.*, **69**, 1562–1581, <https://doi.org/10.1175/JAS-D-11-0220.1>.
- , 2012b: A linear theory of three-dimensional land–sea breezes. *J. Atmos. Sci.*, **69**, 1890–1909, <https://doi.org/10.1175/JAS-D-11-0137.1>.
- Jiang, Z., D. Zhang, R. Xia, and T. Qian, 2017: Diurnal variations of presummer rainfall over southern China. *J. Climate*, **30**, 2755–2773, <https://doi.org/10.1175/JCLI-D-15-0666.1>.
- Kilpatrick, T., S.-P. Xie, and T. Nasuno, 2017: Diurnal convection–wind coupling in the Bay of Bengal. *J. Geophys. Res. Atmos.*, **122**, 9705–9720, <https://doi.org/10.1002/2017JD027271>.
- Li, Y., and R. Carbone, 2015: Offshore propagation of coastal precipitation. *J. Atmos. Sci.*, **72**, 4553–4568, <https://doi.org/10.1175/JAS-D-15-0104.1>.
- Mapes, B. E., T. T. Warner, and M. Xu, 2003: Diurnal patterns of rainfall in northwestern South America. Part III: Diurnal gravity waves and nocturnal offshore convection. *Mon. Wea. Rev.*, **131**, 830–844, [https://doi.org/10.1175/1520-0493\(2003\)131<0830:DPORIN>2.0.CO;2](https://doi.org/10.1175/1520-0493(2003)131<0830:DPORIN>2.0.CO;2).
- Mori, S., and Coauthors, 2004: Diurnal land–sea rainfall peak migration over Sumatera Island, Indonesian maritime continent, observed by TRMM satellite and intensive rawinsonde soundings. *Mon. Wea. Rev.*, **132**, 2021–2039, [https://doi.org/10.1175/1520-0493\(2004\)132<2021:DLRPMO>2.0.CO;2](https://doi.org/10.1175/1520-0493(2004)132<2021:DLRPMO>2.0.CO;2).
- Qian, T., C. C. Epifanio, and F. Zhang, 2009: Linear theory calculations for sea breeze in a background wind: The equatorial case. *J. Atmos. Sci.*, **66**, 1749–1763, <https://doi.org/10.1175/2008JAS2851.1>.
- Rasmussen, K. L., and R. A. Houze Jr., 2011: Orographic convection in subtropical South America as seen by the TRMM satellite. *Mon. Wea. Rev.*, **139**, 2399–2420, <https://doi.org/10.1175/MWR-D-10-05006.1>.
- Romatschke, U., and R. A. Houze Jr., 2010: Extreme summer convection in South America. *J. Climate*, **23**, 3761–3791, <https://doi.org/10.1175/2010JCLI3465.1>.
- Rotunno, R., 1983: On the linear theory of the land and sea breeze. *J. Atmos. Sci.*, **40**, 1999–2009, [https://doi.org/10.1175/1520-0469\(1983\)040<1999:OTLTOT>2.0.CO;2](https://doi.org/10.1175/1520-0469(1983)040<1999:OTLTOT>2.0.CO;2).
- Skamarock, W. C., and J. B. Klemp, 2008: A time-split non-hydrostatic atmospheric model for weather research and forecasting applications. *J. Comput. Phys.*, **227**, 3465–3485, <https://doi.org/10.1016/j.jcp.2007.01.037>.
- Sun, J., and F. Zhang, 2012: Impacts of mountain–plains solenoid on diurnal variations of rainfalls along the mei-yu front over the east China plains. *Mon. Wea. Rev.*, **140**, 379–397, <https://doi.org/10.1175/MWR-D-11-00041.1>.
- Trier, S. B., C. A. Davis, D. A. Ahijevych, M. L. Weisman, and G. H. Bryan, 2006: Mechanisms supporting long-lived episodes of propagating nocturnal convection within a 7-day WRF model simulation. *J. Atmos. Sci.*, **63**, 2437–2461, <https://doi.org/10.1175/JAS3768.1>.
- , —, and R. E. Carbone, 2014: Mechanisms governing the persistence and diurnal cycle of a heavy rainfall corridor. *J. Atmos. Sci.*, **71**, 4102–4126, <https://doi.org/10.1175/JAS-D-14-0134.1>.
- Wang, C. C., G. T. J. Chen, and R. E. Carbone, 2004: A climatology of warm-season cloud patterns over East Asia on GMS infrared brightness temperatures observations. *Mon. Wea. Rev.*, **132**, 1606–1629, [https://doi.org/10.1175/1520-0493\(2004\)132<1606:ACOWCP>2.0.CO;2](https://doi.org/10.1175/1520-0493(2004)132<1606:ACOWCP>2.0.CO;2).
- Wapler, K., and T. P. Lane, 2012: A case of offshore convective initiation by interacting land breezes near Darwin, Australia.

- Meteor. Atmos. Phys.*, **115**, 123–137, <https://doi.org/10.1007/s00703-011-0180-6>.
- Webster, P. J., and Coauthors, 2002: The JASMINE pilot study. *Bull. Amer. Meteor. Soc.*, **83**, 1603–1630, <https://doi.org/10.1175/BAMS-83-11-1603>.
- Yang, G., and J. Slingo, 2001: The diurnal cycle in the tropics. *Mon. Wea. Rev.*, **129**, 784–801, [https://doi.org/10.1175/1520-0493\(2001\)129<0784:TDCITT>2.0.CO;2](https://doi.org/10.1175/1520-0493(2001)129<0784:TDCITT>2.0.CO;2).
- Yang, S., and E. A. Smith, 2006: Mechanisms for diurnal variability of global tropical rainfall observed from TRMM. *J. Climate*, **19**, 5190–5226, <https://doi.org/10.1175/JCLI3883.1>.
- Zhu, L., Z. Meng, F. Zhang, and P. Markowski, 2017: The influence of sea- and land-breeze circulations on the diurnal variability of precipitation over a tropical island (2015). *Atmos. Chem. Phys.*, **17**, 13 213–13 232, <https://doi.org/10.5194/acp-17-13213-2017>.